Marine Structures 41 (2015) 267–287

Contents lists available at ScienceDirect

Marine Structures

journal homepage: www.elsevier.com/locate/marstruc

Time domain approach for coupled cross-flow and in-line VIV induced fatigue damage of steel catenary riser at touchdown zone

Kunpeng Wang [a, b], Wenyong Tang [a, b, *], Hongxiang Xue [a, b]

[a] State Key Laboratory of Ocean Engineering, Shanghai Jiao Tong University, Shanghai 200240, China
[b] Innovation Center for Advanced Ship and Deep-Sea Exploration, Shanghai 200240, China

ARTICLE INFO

Article history:
Received 27 December 2013
Received in revised form 9 December 2014
Accepted 2 February 2015
Available online 13 March 2015

Keywords:
Cross-flow and in-line VIV
Touchdown zone
Linear hysteretic model
Trench shape
Fatigue damage

ABSTRACT

Existing VIV prediction approaches for steel catenary riser (SCR) typically employ truncation model without considering the interaction between the SCR and soil, and only allow for cross-flow (CF) VIV. In this study, a time domain approach accounting for the SCR-soil interaction is proposed to predict the CF and in-line (IL) VIV induced fatigue damage of a SCR at touchdown zone (TDZ). The hydrodynamic force resulting from the vortex shedding is modeled using the forced oscillation test data of a rigid cylinder and an empirical damping model, which are defined as functions of the non-dimensional dominant frequency and amplitude of the SCR response. Due to the coupling effect, the IL VIV force is magnified based on the CF VIV amplitude. By combining a linear hysteretic interaction model with a trench shape model, some particular phenomena during the vertical SCR-soil interaction are captured and qualitatively discussed, while for the horizontal direction, the seabed is simplified as nonlinear spring model. Based on these models, parametric studies are conducted to broaden the understanding of the sensitivity of VIV induced fatigue damage to the seabed characteristic. The results indicate trench depth, vertical and lateral stiffness, and clay suction are significantly affect the VIV induced maximum fatigue damage at TDZ.

* Corresponding author. No.800, Dongchuan Road, School of Naval Architecture, Ocean & Civil Engineering, Shanghai Jiao Tong University, Shanghai 200240, China. Tel./fax: +86 21 34206642.
E-mail address: wytang@sjtu.edu.cn (W. Tang).

http://dx.doi.org/10.1016/j.marstruc.2015.02.004
0951-8339/

1. Introduction

Steel catenary riser (SCR) is a kind of technically feasible and economically efficient structure extensively used in the oil and gas production of deep and ultra-deep water. Due to the restriction of the seabed on the SCR bottom, the touchdown zone (TDZ) is prone to fatigue failure when experiencing oscillations induced by the connected hull response and VIV. Therefore, it is crucial to reasonably simulating the SCR-soil interaction and the relevant environment loads in the design of a SCR. Since the nonlinear hysteretic SCR-soil interaction model was proposed by Aubeny [1] based on STRIDE JIP and CARISIMA JIP [2,3], lots of works [4–6] have been carried out to study the response characteristics of SCRs at TDZ. These studies demonstrated the seabed trench development and its effect on the SCR response near TDP, and the effect of clay suction on the fatigue damage near TDP. Additionally, many researchers [7–10] focused on the laboratory test to study the SCR-soil interaction mechanism, and well captured the mobilization and release of clay suction, which in some extent supported the SCR-soil interaction model.

The prediction technology for the coupled oscillation of the floating hull is already integrated into commercial software, such as DeepC [11], which are widely used in the offshore industry. In regards to the VIV, although the basic mechanism is well known [12], and relevant experimental studies using spring mounted rigid cylinder [13–15] and large scale riser models [16–20] have been extensively investigated, a reliable approach for the simulation of riser VIV in time domain is still needed. Owing to the complex fluid–structure interaction mechanism, the current VIV prediction approaches are limited to CF VIV, and are mostly in frequency domain [21,22]. Baarholm [23] indicated that IL VIV causes as much fatigue damage as CF VIV, and cannot be neglected. Frequency domain approach is cost efficient, but SCR-soil interaction and other nonlinear boundary conditions cannot be well taken into account. In recent years, more attentions are paid to time domain approach, and some codes are developed, such as ABAVIV [24] and SimVIV [25]. However, these codes cannot consider the IL VIV, or apply simple hydrodynamic coefficient in the IL direction. In regards to VIV induced fatigue damage at TDZ, a series of studies were carried out in time domain by Larsen et al. [26] and Wang et al. [27], while also limited to CF VIV.

Based on the forced vibration test data [28,29], this paper proposed a time domain approach to simulate the coupled CF and IL VIV, and validate it using the Hanøytangen riser model. The comparison of the numerically and experimental obtained displacement RMS and fatigue damage indicates this approach can reasonably predict riser VIV response. The fatigue damages are both calculated using rain flow counting methodology. Combined with a SCR-soil interaction model considering the clay suction and trench shape in vertical direction, and lateral seabed stiffness, the time domain VIV approach is used to study the sensitivity of fatigue damage of a SCR at TDZ on the seabed characteristics, and some useful conclusions are obtained.

2. Coupled CF and IL VIV model

2.1. Model formulation

SCR is a kind of slender structure connecting vessel and seabed, see Fig. 1. The response of a SCR exposed in the ocean current can be expressed using the Euler–Bernoulli equation as follows:

$$m\ddot{r} + c\dot{r} + \left(EIr''\right)'' - (T_e r')' = F_{Hydro} + F_{soil} \tag{1}$$

where r is the position vector, m is the riser mass per unit length, c is the structural damping, EI is the bending stiffness, T_e is the effective tension, F_{Hydro} is the hydrodynamic force, F_{soil} is the seabed resistance.

Periodic vortex shedding at the two side of the SCR induces the hydrodynamic force in two directions transverse and align with the flow, which cause the CF and IL VIV respectively. The hydrodynamic force is in general decomposed into the velocity-related item F_V, and the accelerate-related item F_M [29]. Therefore, F_{Hydro} can be expressed as:

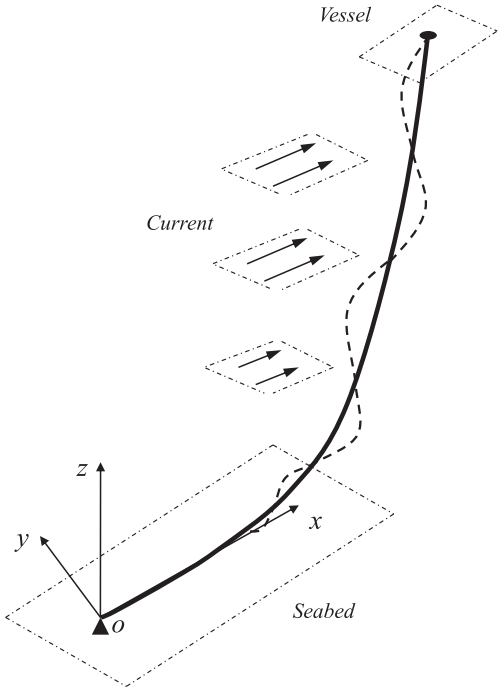

Fig. 1. Configuration of the steel catenary riser.

$$F_{Hydro} = \begin{Bmatrix} F_{V,CF} \\ F_{V,IL} \end{Bmatrix} + \begin{Bmatrix} F_{M,CF} \\ F_{M,IL} \end{Bmatrix} \tag{2}$$

where the subscripts 'CF' and 'IL' represent the CF and IL related items respectively.

Considering the similar formula type, F_V and F_M in the CF and IL directions are uniformly given as follows:

$$F_V = \frac{1}{2}\lambda C_V(A^*, f_r)\rho_f D V^2 \cos(\omega t) \tag{3}$$

$$F_M = \frac{\pi}{4} C_M(A^*, f_r)\rho_f D^2 \omega^2 A \sin(\omega t) = -m_a \ddot{r} \tag{4}$$

where $C_V(A^*, f_r)$ and $C_M(A^*, f_r)$ is excitation coefficient and added mass coefficient, λ is the amplification factor of the excitation coefficient due to coupling effect, $A^* = A/D$ is non-dimensional amplitude, $f_r = f_d D/V$ is dominant non-dimensional frequency, f_d is dominant frequency of a riser response described in Section 2.2, ρ_f is fluid density, D is riser diameter, V is current velocity, A is response amplitude, $\omega = 2\pi f_d$ is circular frequency, m_a is added mass per unit length. By default the above parameters not only represent the CF items but also IL items, unless the subscript 'CF' and 'IL' are added to. For example, $C_{V,IL}(A^*_{IL}, f_{r,IL})$ only denotes the IL excitation coefficient.

The CF and IL excitation coefficients are obtained by Gopalkrishnan [28] and Aronsen [29] respectively based on the forced vibration test of rigid cylinder. Figs. 2 and 3 demonstrate the excitation coefficients as a function of non-dimensional amplitude and dominant non-dimensional frequency. In the present study, the added mass coefficient is taken to be 1.0.

The CF and IL VIV have coupling effect, and influence each other. Blevins [12] indicated that when CF amplitude exceeds 0.2–0.3 riser diameters, the CF response can significantly amplify the IL response.

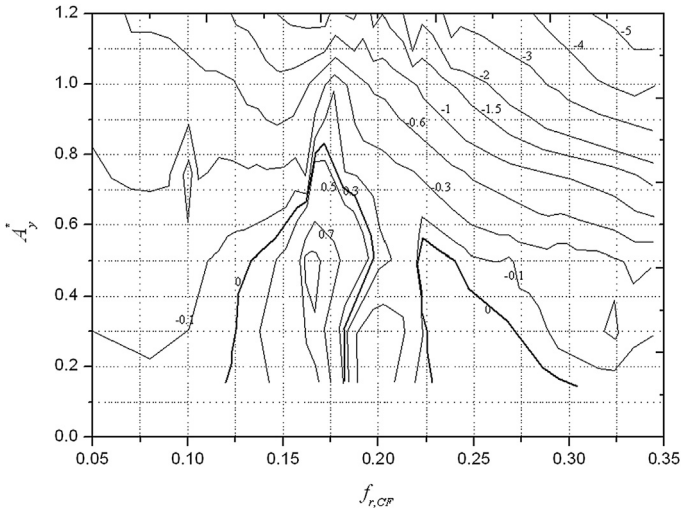

Fig. 2. CF excitation coefficient, $C_{V,CF}$ [28].

Fig. 4 shows the amplification factor of IL excitation coefficient as a function of the ratio of CF amplitude to riser diameter. Since the widely used frequency domain codes can give reasonable and acceptable prediction without considering the effect of IL response on CF response, the amplification factor of CF excitation coefficient is simply set to 1.0.

Generally, positive excitation coefficient denotes the excitation force synchronize to the riser's velocity, while negative value means hydrodynamic damping. The associated damping coefficient can be obtained based on the assumption of equivalent dissipated power in a period:

$$c_f = -\frac{C_V \rho_f V^2 D}{2A\omega} \tag{5}$$

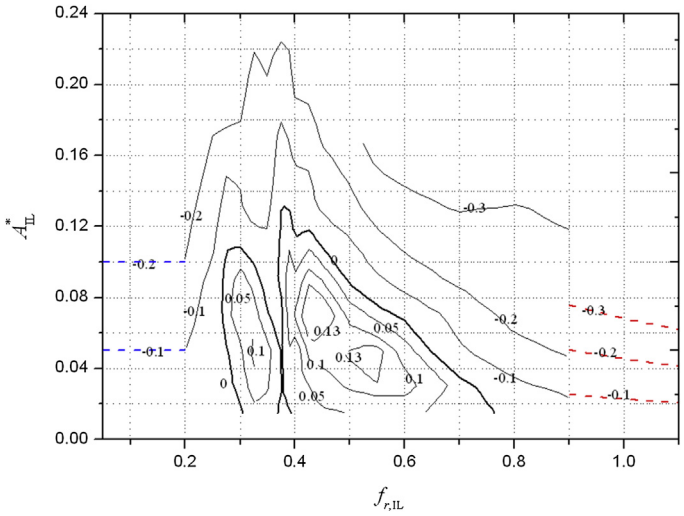

Fig. 3. IL excitation coefficient, $C_{V,IL}$ [29].

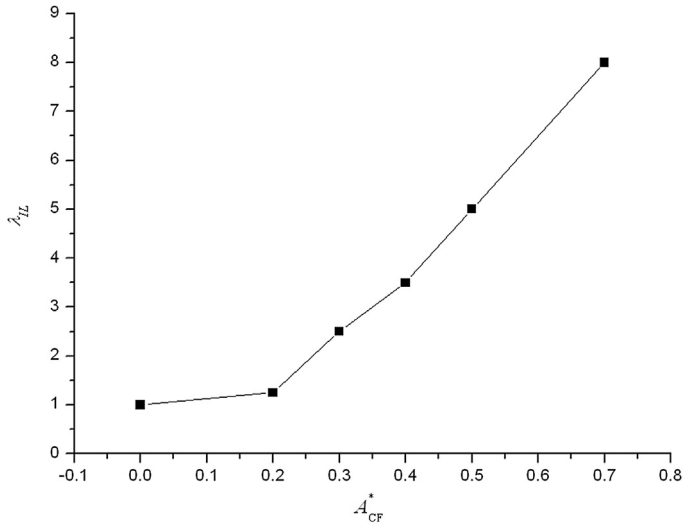

Fig. 4. Amplification factor of IL excitation coefficient [12].

Outside the test range, the empirical damping model for CF VIV proposed by Venugopal [30] is used, which classifies the hydrodynamic damping according to the dominant non-dimensional frequency region.

Damping in high dominant non-dimensional frequency region:

$$c_f = C_{hf}\rho_f DV + c_{sw} \tag{6}$$

where C_{hf} is taken to be 0.18 [21]. C_{sw} is the still water damping given by:

$$c_{sw} = \frac{\omega\pi\rho_f D^2}{2}\left[2\sqrt{\frac{2}{\omega D^2/\nu}} + C_{sw}\left(\frac{A}{D}\right)^2\right] \tag{7}$$

where ν is the kinematic viscosity of the fluid, and $C_{sw} = 0.2$ [21].

Damping in low dominant non-dimensional frequency region:

$$c_f = C_{lf}\rho_f V^2 \Big/ \omega \tag{8}$$

where C_{lf} is taken to be 0.2 [21].

In this study, the IL VIV also uses the above hydrodynamic damping model with different empirical parameter values due to different oscillation direction and vortex shedding mode. By matching the extension of the contour of the IL excitation coefficient, the C_{hf} and C_{lf} are set to be 0.35 and 1.0 respectively. The dash lines in Fig. 3 show the extended contour calculated using the damping model.

2.2. Determination of amplitude and dominant frequency

The amplitude and dominant frequency of a riser element are essential to obtained hydrodynamic force. In the CF and IL direction, the displacement, time and velocity (corresponding to the symbols: u, t, v) at each step are extracted. According to the adjacent two points a and b with $v = 0$, the calculated amplitude and frequency can be determined by: $A_c = |u_b\text{-}u_a|/2$, $f_c = 1/(2 \times (t_b - t_a))$. In this study, the calculated amplitude is considered as the above mentioned amplitude: $A = A_c$.

To obtain the dominant frequency of each riser element, the following steps are undertaken:

(a) Determination of the excitation region $[f_{r1}, f_{r2}]$ and the region center for CF and IL VIV respectively. The excitation region is defined according to Figs. 2 and 3. The region center is the f_r corresponding to the maximum excitation coefficient. CF VIV has one excitation region with range of [0.125, 0.2] [22], while IL VIV has two excitation regions with range of [0.27, 0.375] and [0.375, 0.76] respectively [29]. The related center is 0.17 for CF VIV, and 0.33 and 0.43 for IL VIV. Noted that above values changes with variation of Strouhal number as equation (9):

$$\left(\frac{f_r}{S_t}\right)_{test} = \left(\frac{f_r}{S_t}\right)_{actual} \tag{9}$$

(b) The natural frequency closer to the frequency associated with the region center is chosen as the preliminary dominant frequency, and then initial amplitude is assumed for each element in two directions to obtain the hydrodynamic force to drive the riser response.
(c) Based on the response, A_c and f_c are calculated. If the non-dimensional frequency associated with f_c falls in the corresponding excitation regions, e.g. $\frac{f_c D}{V} \in [f_{r1,CF}, f_{r2,CF}]$ for CF VIV, the natural frequency closer to the region center, i.e. the preliminary dominant frequency, would dominate the riser element response, and lock-in occurs; if outside the range, f_c is considered as the dominant frequency, and the riser element is subjected to damping force.
(d) At the end of each incremental step, step (c) is conducted to determine the dominant frequency for the next incremental step.

According to above statement, a riser element in IL VIV may be locked in at two frequencies, e.g. $f_{1,IL}$ and $f_{2,IL}$ corresponding to the two excitation regions respectively. If this happens, the proposed

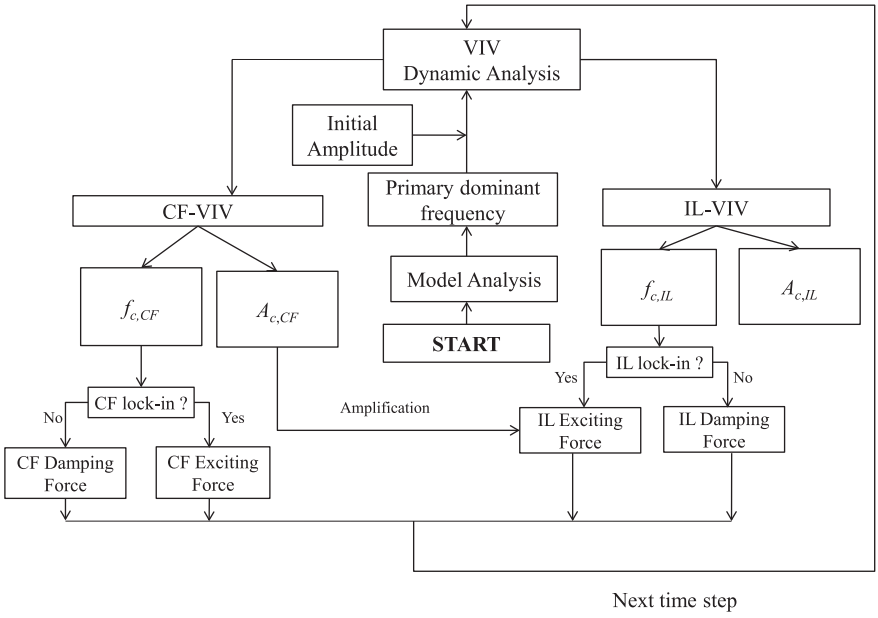

Fig. 5. Flowchart of VIV analysis.

Table 1
Parameters of HanØtangen's riser model.

Parameters	Value
Length (m)	90
Out diameter (m)	0.03
Inner diameter (m)	0.026
Young's modulus (Pa)	2.1×10^{11}
Mass ratio	3.13
Structural damping	0.003
Top tension (N)	3700

approach divides A_c into two parts, A_{c1} and A_{c2}, and assigns them to the two lock-in modes. The criterion of determining the values of A_{c1} and A_{c2} is that the combination of the excitation forces, $C_{V,IL}(A_{c1}/D, f_{1,IL}D/V) + C_{V,IL}(A_{c2}/D, f_{2,IL}D/V)$ is maximum. For understandability, Fig. 5 demonstrates the flowchart of VIV analysis.

2.3. Validation based on large scale riser model

The riser model used in Hanøytangen test [23,31] is simulated to validate the present approach. In the test, the riser is exposed in a linear sheared current profile by moving the vehicle at a constant speed. The tension is kept constant by the buoyancy device. The riser properties are presented in Table 1. In this study, the Strouhal number is taken to be 0.17.

The RMS of displacement is first compared for the case with the vehicle speed of 0.54 m/s. Figs. 6 and 7 illustrate the numerical and experimental results. It is noted that the present approach gives a higher prediction at the upper zone of the riser. At the bottom zone, the results show good agreement for CF VIV, while the present numerical IL VIV result is underestimated. The tendency of the displacement profile can exhibit the dominant mode. For CF VIV, mode 11 approximately dominates the riser response for both method, while for IL VIV, the present approach predicts mode 20 as the dominant mode, lower than the mode 23 of the experimental result.

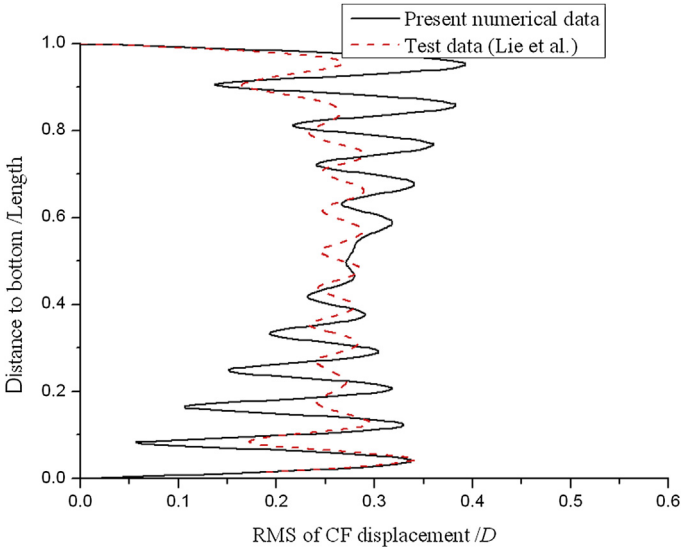

Fig. 6. Comparison of CF displacement RMS.

Based on the stress time histories, the fatigue damages are obtained using rain flow counting methodology, as shown in Figs. 8 and 9. S–N curve parameters are listed in Baarholm [23]. In the present study, only sixty points uniformly along the riser is calculated and the associated stress is considered as a combination of bending stress and axial stress [32]. The results indicated that except for the upper zone, the present approach gives lower estimate, especially at the middle zone for IL VIV. Overall, the present approach is reasonable for the coupled VIV response prediction, and when combined with rain flow counting methodology, can give reasonable fatigue life.

3. SCR-soil interaction model

3.1. Model formulation

With continuous impact of the SCR on the seabed, a seabed trench generates and develops. The study by 2H Offshore [33] indicates that whether or not considering the trench shape has significant effect on the prediction of a SCR at TDZ. Bridge [34] reported several observed trench shape in Gulf of Mexico, which showed that SCR trenches in general have ladle shape in profile. Based on this, a trench shape model in vertical direction is proposed, and the ladle shaped part is divided to linear, nonlinear and extended zones, seen Fig. 10. As an attempt, the trench corresponding to the buried zone of a SCR is related with the maximum penetration, riser diameter and mass per unit length. The horizontal length l_B and l_L, and the slope angle α of the linear zone are given as [27]:

$$\begin{aligned} l_B &= \gamma\sqrt{|z|_{\max}/D}\Big/ m^{1/3} \\ l_L &= \frac{\sqrt{|z|_{\max}/D}}{1+\varphi\sqrt{|z|_{\max}/D}}\varphi l_B \\ \alpha &= atg\left(\beta\sqrt{|z|_{\max}/D}\right) \end{aligned} \tag{10}$$

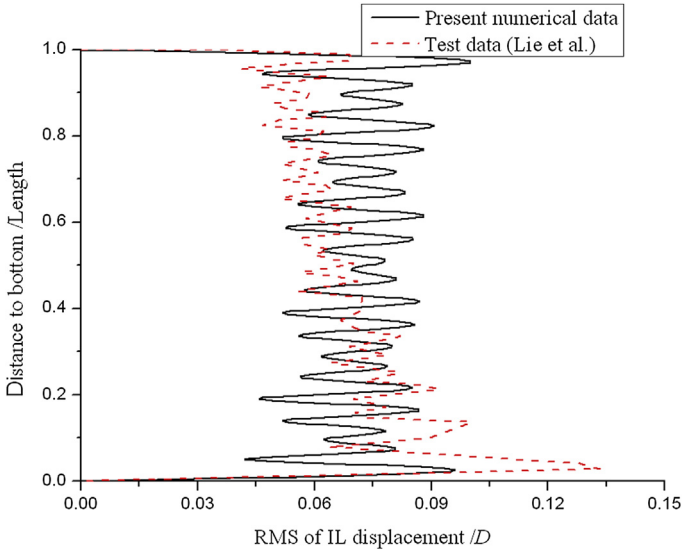

Fig. 7. Comparison of IL displacement RMS.

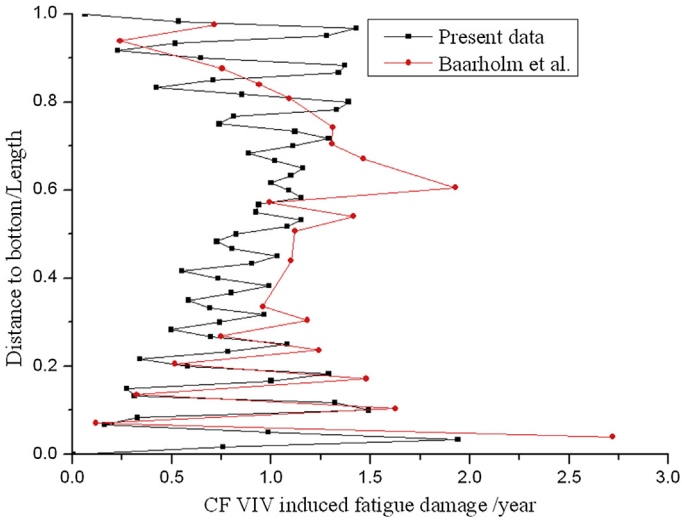

Fig. 8. Comparison of CF VIV induced fatigue damage.

where $|z|_{max}$ is the maximum penetration in a trench, γ, φ and β are empirical trench shape parameters.

The nonlinear zone is depicted by equation (11):

$$d^4|z|\Big/dx^4 = 0 \tag{11}$$

By setting rotation angle to be zero at the maximum penetration position and α at the other end, the nonlinear zone can be obtained. As for the extended zone, this paper simply employs the mirror symmetry of the nonlinear zone. The penetration corresponding to the surface zone of a SCR is

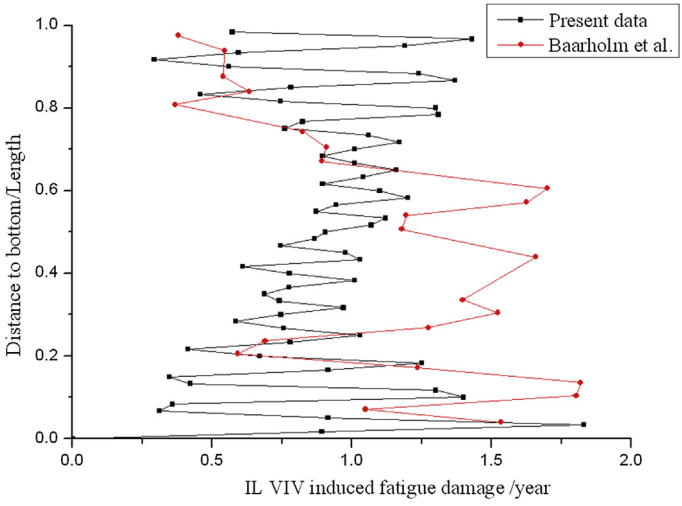

Fig. 9. Comparison of IL VIV induced fatigue damage.

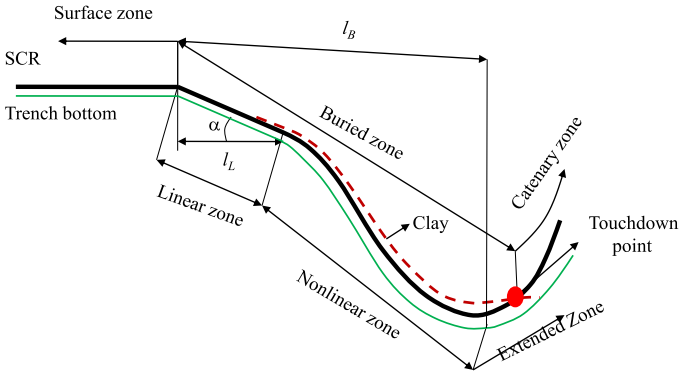

Fig. 10. Sketch of seabed trench.

determined by equating the riser submerged weight to the soil resistance, P_z, governed by the backbone curve given as:

$$P_z = N_P D(S_0 + S_g|z|) \tag{12}$$

where S_0 and S_g are mudline shear strength and shear strength gradient respectively, $|z|$ is the penetration of a SCR into seabed. N_p is a dimensionless bearing factor expressed as:

$$N_P = a(|z|/D)^b \tag{13}$$

where a and b are empirical parameters taken to be 6.7 and 0.254 respectively [1].

Bridge [2] described the SCR-soil interaction process as a full loop enclosed by the black line in Fig. 11, and proposed soil stiffness model considering soil suction and conservative large displacement soil stiffness model represented by dash line ② and dot dash line ④ respectively. This study simulates the SCR-soil interaction with linear hysteretic model depicted by the loop: ①→②→③ [6,27]. When the SCR

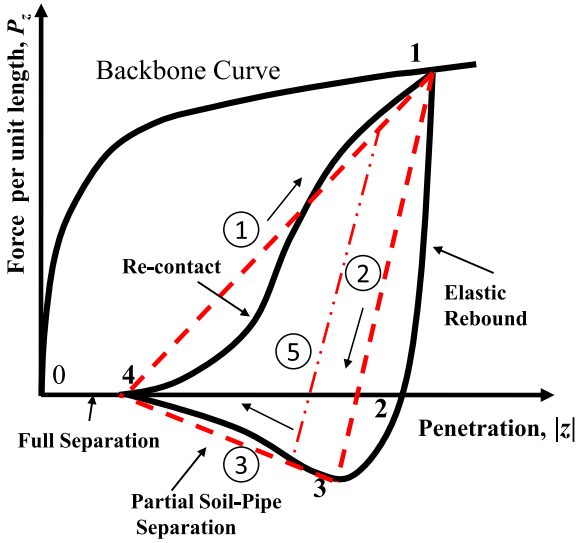

Fig. 11. Sketch of SCR-soil vertical interaction process.

Table 2
Parameters of SCR-soil interaction model.

Particulars	Definition
$\|z\|_{max}$	Maximum depth of trench for beam-spring model
S_0	Seabed mudline shear strength
S_g	Seabed shear strength gradient
μ_{sep}	Riser-soil separation factor $\|z\|_4/\|z\|_1$
λ_{suc}	Position factor of maximum suction $(\|z\|_3-\|z\|_4)/(\|z\|_1-\|z\|_4)$
f_{suc}	Maximum suction factor $-P_{z,3}/P_{z,1}$
γ	Empirical parameter for trench shape
φ	Empirical parameter for trench shape
β	Empirical parameter for trench shape
$k_{L,max}$	Lateral stiffness of the seabed at point 1

uplift, the soil resistance decreases to zero at point 2, and then the clay suction mobilizes and then releases following: 2 → 3 → 4. When the SCR contacts with seabed again, the soil resistance appears and increases from points 4 to 1. If reverse motion occurs without reaching point 1 when the SCR moves downwards or without SCR-soil separation when the SCR moves upwards, the $P_z-|z|$ relation yields to double dot dash line ④ parallel with dash line ②.

Different position along TDZ has different loop determined by related points 1, 3 and 4. The seabed resistance $P_{z,1}$ at point 1 is obtained by assigning the relevant trench depth to $|z|$ in equation (12). Point 3 is related with the seabed suction, which is determined by two parameters: λ_{suc} for the related penetration, and f_{suc} for the maximum suction. Point 4 is the position where the SCR separates from seabed, determined by parameter μ_{sep}.

For the lateral interaction, a spring model considering SCR-soil separation is employed. To avoid large variation of lateral force when SCR-soil separation, the model stiffness is assumed to linearly decrease from $k_{L,max}$ (at point 1) to 0 (at point 4).

As a summary, the related parameters controlling the SCR-soil interaction model are presented in Table 2.

3.2. Identification for the trench shape parameters

This section employed the observed trenches of two SCRs in Bridge [34] to determine the trench shape parameters. The selected SCRs have the same out diameter and wall thickness: $D = 0.3239$ m, $t = 0.0175$ m. Based on equation (10) and the observed trench dimensions in Table 3, the trench shape parameters are calculated, and approximately taken to be: $\gamma = 122$, $\varphi = 0.27$ and $\beta = 0.016$. The numerical and observed trenches corresponding to the two SCRs are plotted in Figs. 12 and 13, where the linear zone is in good agreement, whereas the nonlinear zone is slightly over estimated. It should be mentioned that the self-weight penetration is very small, so it is not considered in the two figures.

Table 3
Trench dimensions and shape parameters.

	Gas export SCR	Oil export SCR
l_B (m)	50.4	31
l_L (m)	17.5	8.4
α (deg)	1.96	1.25
$\|z\|_{max}$ $(/D)$	4.3	2.1
γ	123.5	121.0
φ	0.272	0.263
β	0.0163	0.0151

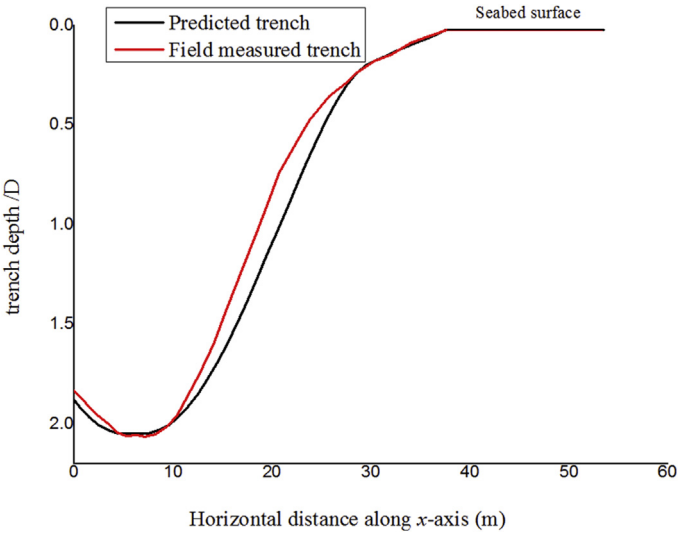

Fig. 12. Trench shape comparison of oil export SCR.

3.3. *Qualitative analysis for the linear hysteretic model and lateral stiffness model*

Although many studies have been carried out for SCR-soil interaction, model considering seabed trench is barely found in the published literatures. Therefore, this paper only qualitatively discusses the obtained P_z–$|z|$ and P_y–y relations in the simulation of the targeted SCR. The SCR properties and environment parameters are presented in Section 4.1. The parameters of the SCR-soil model are: $|z|_{max} = 0.6$ m, $S_0 = 3.5$ kPa, $S_g = 2.5$ kPa/m, $\mu_{sep} = 0.6$, $\lambda_{suc} = 0.8$, $f_{suc} = 0.2$, $\gamma = 122$, $\varphi = 0.27$, $\beta = 0.016$, $k_{\mathrm{L,max}}$ is simply taken to be k_1 (k_1 is the stiffness corresponding to line ① in Fig. 11).

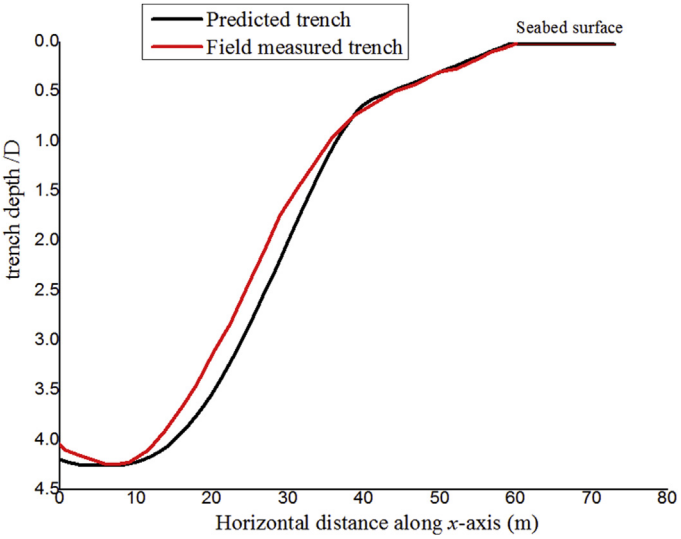

Fig. 13. Trench shape comparison of gas export SCR.

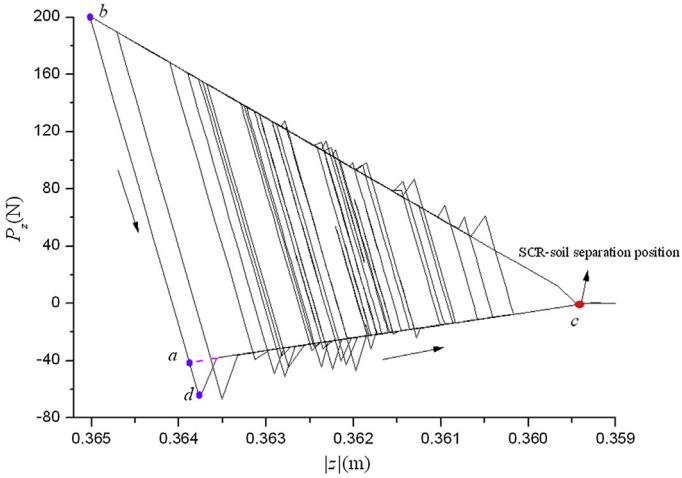

Fig. 14. P_z-$|z|$ relation at node 189.

SCR-soil interaction forces at node 189 between the maximum penetration position (node 186) and touchdown point (TDP, node 192) are extracted. $P_z-|z|$ relation is plotted in Fig. 14. It is seen that SCR separates with seabed at point *c*. Owing to that P_z changes based on the displacement and velocity of the former calculation step, the clay suction do not turn to release immediately at point *a*, but reaches a higher value at point *b*, and then decreases to the expected $P_z-|z|$ relation ($a \rightarrow c$). Additionally, it is noted that the clay suction at point *a* is 0.2 times soil resistance at point *b* as expected. The lateral seabed stiffness keeps changing with up-and-down motion of the SCR, which causes nonlinear P_y-y curve, see Fig. 15. The point with P_y equal to 0 is the SCR-soil re-contact position, such as points *e*, *g* and *g*.

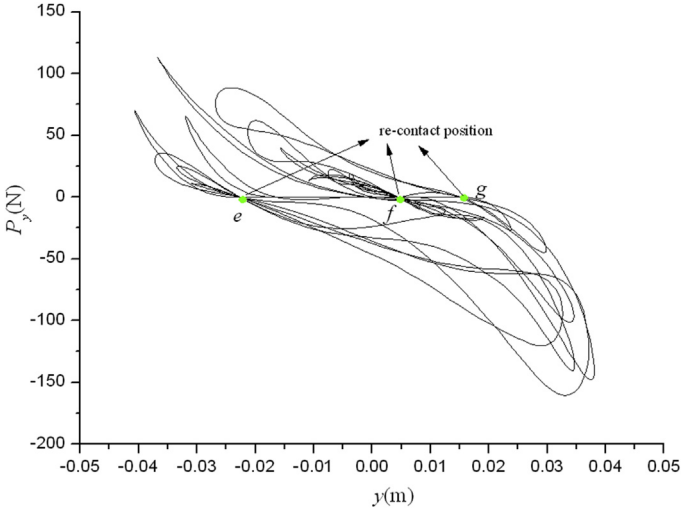

Fig. 15. P_y-y at node 189.

Table 4
Principles of the targeted SCR.

Length	1410.8	m
Horizontal span	791	m
D	0.3	m
t	0.016	m
Mass per unit length	112	kg
Height of top hang off point	975	m
Hang off angle	12	deg

4. Fatigue sensitivity analysis

4.1. Model parameters

The targeted SCR serves in a semi-submersible platform system in the sea area with water depth of 1000 m. Its properties are presented in Table 4. Fig. 16 gives the current component perpendicular to the SCR since this component accounts for VIV. In this study, the current is taken in the xz-plane.

For the purpose of investigating the sensitivity of the fatigue damage of the SCR at TDZ to the seabed characteristics, five cases with variation of (1) $|z|_{\max}$, (2) S_0, (3) S_g, (4) f_{suc} and (5) $k_{L,\max}$ are simulated. The related parameters of SCR-soil interaction model are presented in Table 5 $k_{L,\max}$ is taken as the multiples of k_1.

4.2. Modal analysis

The aim of modal analysis is to calculate the natural frequencies in CF and IL direction respectively. Based on the obtained natural frequencies, VIV analysis can be carried out. To demonstrate the dominant frequencies, the amplitude spectrum of VIV response ate node 189 is calculated. Fig. 17(a) shows that the dominant frequency of CF VIV is 0.47 Hz, while due to existence of two excitation regions, the IL VIV has two dominate frequencies approximately equal to 0.93 Hz and 1.22 Hz respectively, see Fig. 17(b).

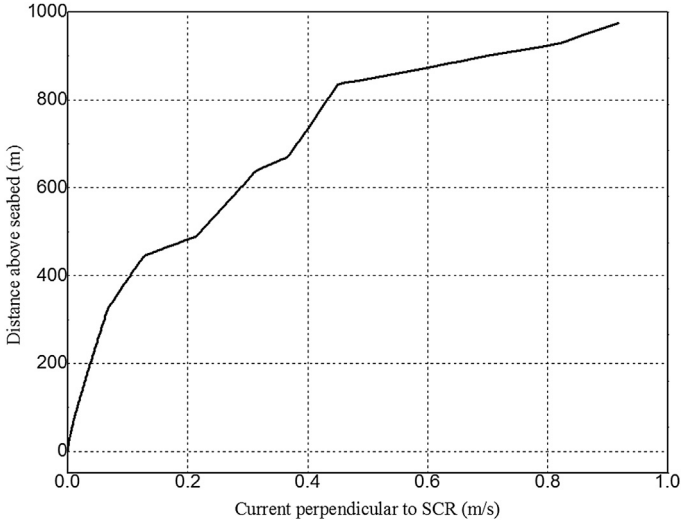

Fig. 16. Current component perpendicular to the SCR.

Table 5
Summary of seabed parameter values.

Parameters	Case number				
	1	2	3	4	5
$\|z\|_{max}$	0.2, 0.3, 0.4, 0.5, 0.6, 0.7, 0.8	0.6	0.6	0.6	0.6
S_0	1.5	1, 2, 3, 3.5	1.5	1.5	1.5
S_g	2.5	2.5	1.5, 2.5, 3.5, 4.5	2.5	2.5
μ_{sep}	0.6	0.6	0.6	0.6	0.6
λ_{suc}	0.8	0.8	0.8	0.8	0.8
f_{suc}	0.2	0.2	0.2	0.2,0.25, 0.3, 0.4, 0.6	0.2
γ	122	122	122	122	122
φ	0.27	0.27	0.27	0.27	0.27
β	0.016	0.016	0.016	0.016	0.016
$k_{L,max}$	1	1	1	1	1, 2, 4, 6, 8, 10, 20

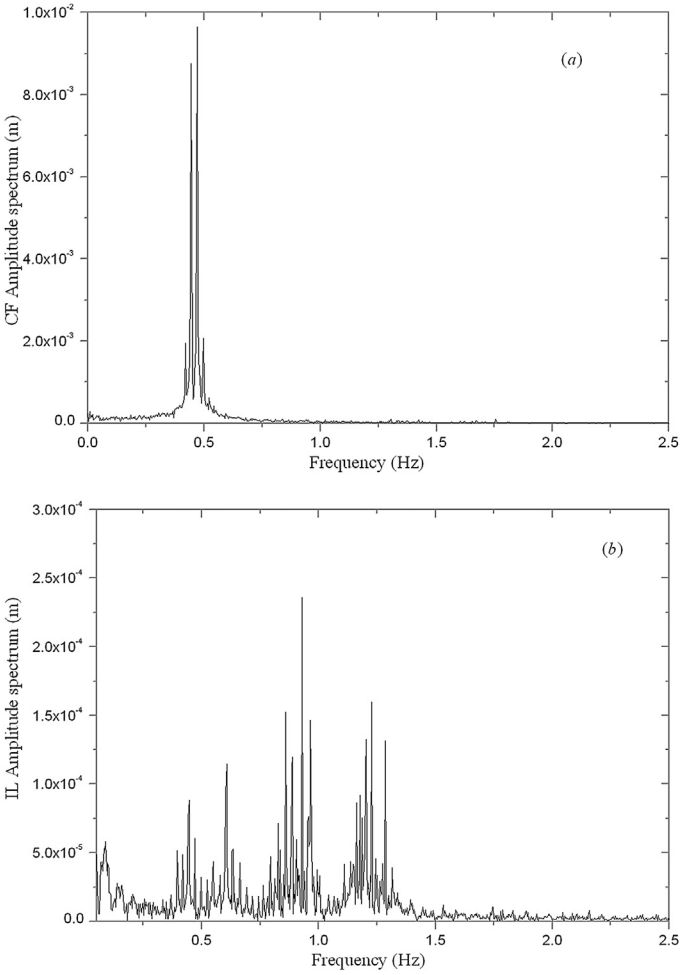

Fig. 17. Amplitude spectrum of VIV response at node 189.

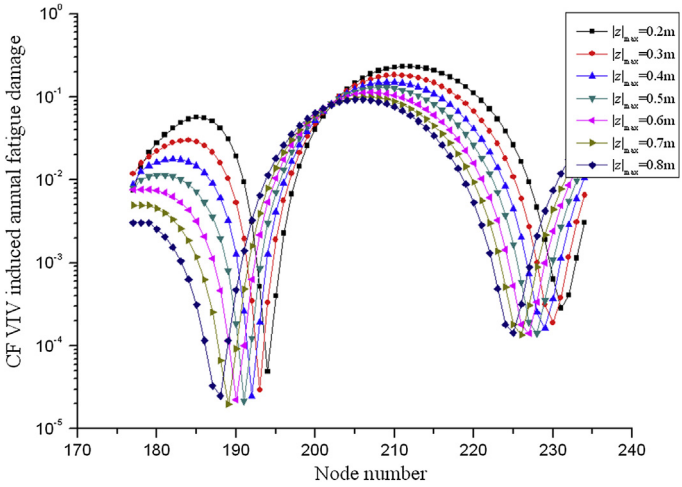

Fig. 18. CF VIV induced annual fatigue damage.

4.3. Results and discussion

4.3.1. Trench depth

Continuous contact between SCR and seabed can cause trench development. This study simulates trenches with different depth by changing $|z|_{max}$. Figs. 18 and 19 illustrate the VIV induced annual fatigue damage. Different from the vessel oscillation induced fatigue damage, the maximum value along TDZ is smaller than that along the catenary zone. By default the fatigue damage in the following context refers to the maximum fatigue damage at TDZ.

As trench becomes deeper, the position of CF VIV induced maximum fatigue damage moves left obviously, while the position of IL VIV nearly remains constant. Fig. 20 shows that CF and IL VIV induced maximum fatigue damages decrease with trench development. For shallow trench, the maximum fatigue damage of CF VIV is apparently larger than that of IL VIV. However, trench development can diminish the difference, and even make the latter larger.

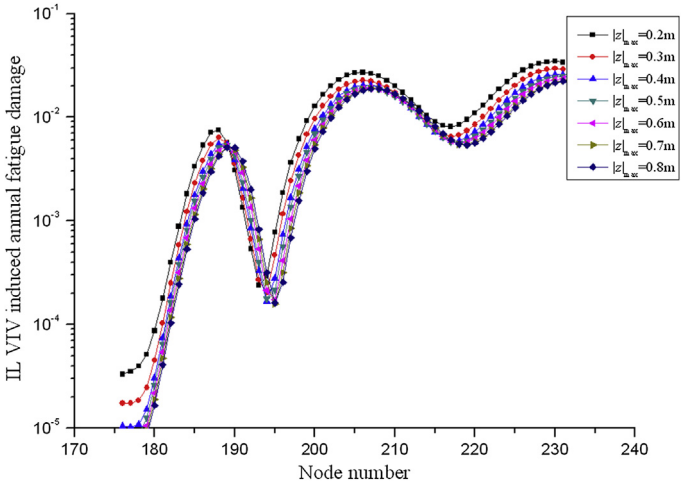

Fig. 19. IL VIV induced annual fatigue damage.

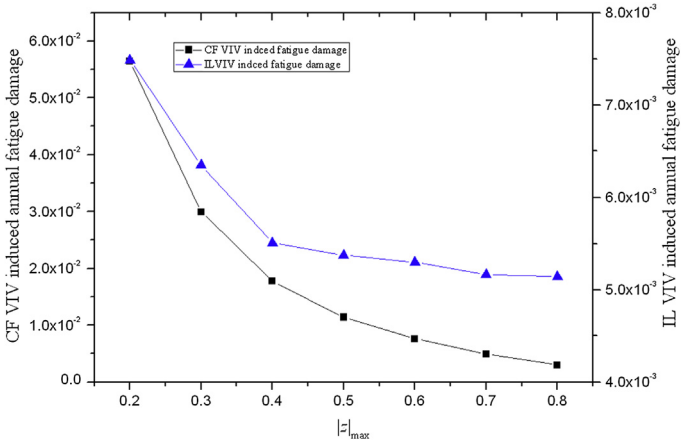

Fig. 20. Maximum fatigue damage along TDZ.

4.3.2. Mudline shear strength and shear strength gradient

Higher mudline shear strength and shear strength gradient corresponding to stiffer seabed give higher maximum annual fatigue damage, see Figs. 21 and 22. The CF and IL VIV induced fatigue damages both almost linearly increase with increasing mudline shear strength and shear strength gradient. When the mudline shear strength increases from 1.0 to 3.5 kPa, the increments of the CF and IL fatigue damage are 2.16×10^{-3} and 1.42×10^{-3} respectively. When the shear strength gradient increases from 1.5 to 4.5 kPa/m, the increments of the CF and IL fatigue damage are 8.4×10^{-4} and 1.26×10^{-3} respectively. Therefore, the ratios of CF and IL fatigue damage to mudline shear strength approximately equal 8.64×10^{-4} ($2.16 \times 10^{-3}/2.5$) and 5.68×10^{-4} ($1.42 \times 10^{-3}/2.5$) respectively, while the ratios to shear strength gradient are 2.8×10^{-4} ($8.4 \times 10^{-4}/3$) and 4.2×10^{-4} ($1.26 \times 10^{-3}/3$). This indicates that the fatigue damage is more sensitive to the mudline shear strength, especial for CF VIV.

4.3.3. Clay suction

Clay suction is a special phenomenon, which is well captured by the present SCR-soil interaction model. It should be noted that the clay suction of this model only corresponds to the vertical

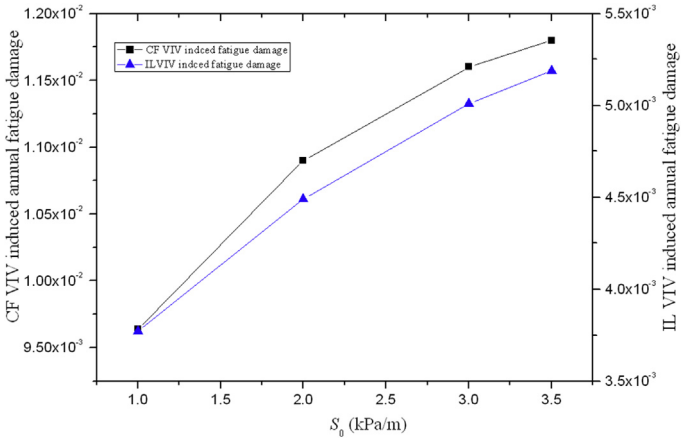

Fig. 21. Maximum fatigue damage along TDZ vs. S_0.

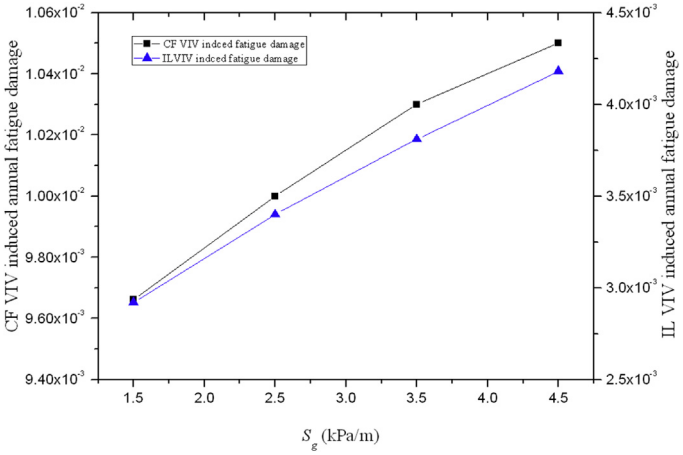

Fig. 22. Maximum fatigue damage along TDZ vs. S_g.

response. Fig. 23 shows its effect on the CF and IL fatigue damage. It is noted that the variation of CF fatigue damage is very little, while for IL VIV, the growth rate of fatigue damage is 53.7%. Therefore, the clay suction has barely effect on the lateral response, but significantly changes the vertical response.

4.3.4. Seabed lateral stiffness

So far there is not a relative sophisticated approach to simulate the lateral SCR-soil interaction. This section is to investigate the effect of the seabed lateral stiffness on the CF and IL fatigue damage. Figs. 24 and 25 show that higher lateral stiffness corresponding to harder horizontal restriction makes the position of CF maximum fatigue damage closer to TDP, while the position almost remains constant for IL VIV. Fig. 26 illustrates the maximum fatigue damage at TDZ vs. seabed lateral stiffness. It is noted that the seabed lateral stiffness not only has significant effect on the CF fatigue damage, but also severely affects the IL fatigue damage. Therefore, it is crucial to reasonably model the SCR-soil lateral interaction for accurate prediction of fatigue damage of a SCR.

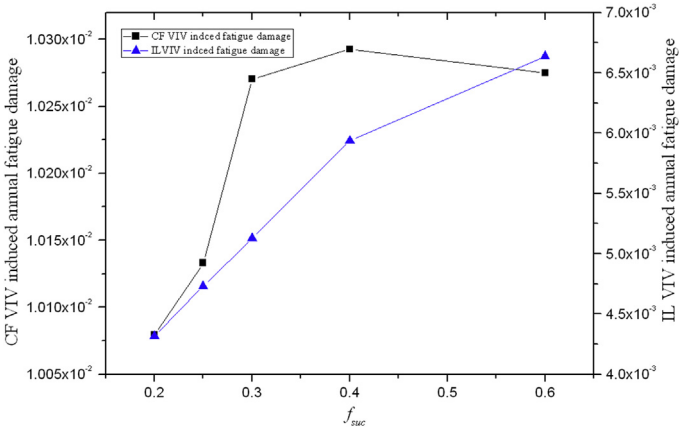

Fig. 23. Maximum fatigue damage along TDZ vs. f_{suc}.

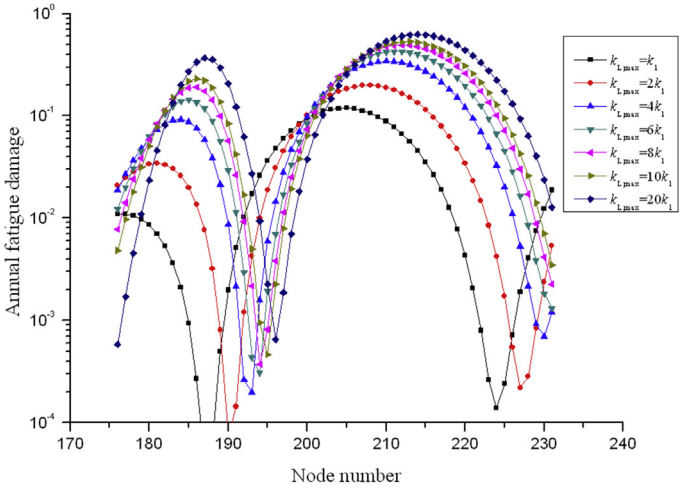

Fig. 24. CF fatigue damage vs. node number.

5. Conclusions

A time domain approach for coupled CF and IL VIV prediction has been proposed. The riser model of Hanøytangen is used to validate it by comparison of displacement and annual fatigue damage. The results show good agreement. To broaden the understanding of VIV induced fatigue of SCR, especially along TDZ, a SCR-soil interaction model considering the trench shape, clay suction and seabed lateral stiffness are integrated with the VIV prediction approach, and a targeted SCR is simulated. Considering the indispensability of natural frequencies in VIV analysis, Modal analysis is first conducted. The mode shape denotes that only modes in or perpendicular to SCR plane are apt to be excited. Additionally, except for low order modes, two adjacent modes in and perpendicular to SCR plane generally have the equal frequency. Parametric studies are then carried out to investigate

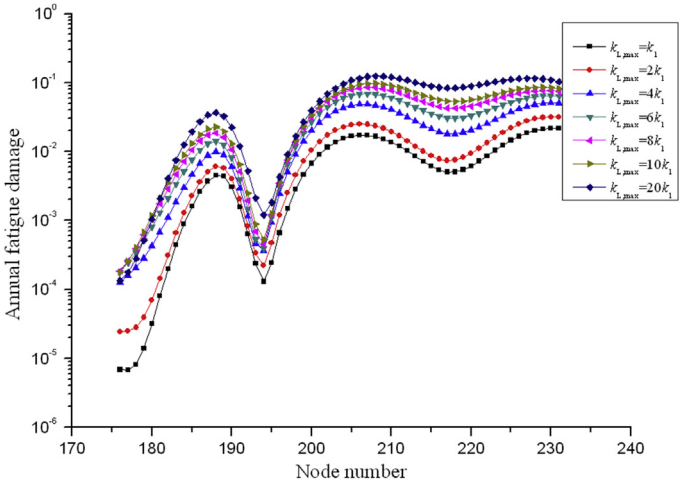

Fig. 25. IL fatigue damage vs. node number.

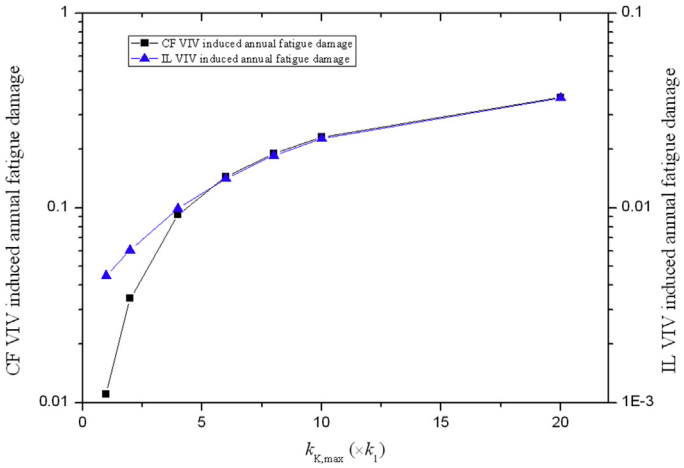

Fig. 26. Maximum fatigue damage along TDZ vs. f_{suc}.

the effect of seabed characteristics on the fatigue damage of the SCR along TDZ, and some conclusions are obtained:

(1) For this SCR, CF and IL VIV induced maximum fatigue damages both decrease with trench development. When seabed trench is shallow, CF VIV induced maximum fatigue damage is obviously larger than IL VIV. However, as trench becomes deeper, the difference reduces, and inverse result even occurs.
(2) CF and IL VIV induced maximum fatigue damages increase with increment of mudline shear strength and shear strength gradient. The sensitivity of the maximum fatigue damage to mudline shear strength slightly decreases, whereas the maximum fatigue damage has nearly linear relationship with shear strength gradient.
(3) Due to CF VIV perpendicular to SCR plane, clay suction barely affects the related maximum fatigue damage. However, IL induced maximum fatigue damage increases obviously with increasing clay suction.
(4) Larger seabed lateral stiffness gives higher CF and IL VIV induced maximum fatigue damage, and makes the position of CF VIV induced fatigue damage closer to TDP. However, the maximum fatigue damage position of IL VIV almost remains constants with variation of lateral stiffness.

Finally, it should be noted that VIV induced maximum fatigue damage of the whole SCR is not located at TDZ. Next work will focus on the combination of VIV and vessel oscillation induced fatigue damage, and identifies the critical position.

Acknowledgment

This paper is based on the projects supported by the National Natural Science Foundation of China (Grant No. 51490674).

References

[1] Aubeny CP, Biscontin G, Zhang J. Seafloor interaction with steel catenary risers. Report. Texas A&M University; 2006.
[2] Bridge C, Laver K. Steel catenary riser touchdown Point vertical interaction models. In: Offshore technology conference, Houston, Texas, USA; 2004.
[3] Marintek. CARISIMA, Interpretation of suction test results. Report No. 700039.00.03, Trondheim, Norway. 2000.
[4] Nakhaee A, Zhang J. Trenching effects on dynamic behavior of a steel catenary riser. Ocean Eng 2010;37:277–88.

[5] Randolph M, Quiggin P. Non-linear hysteretic seabed model for catenary pipeline contact. In: Proceedings of the ASME 28th international conference on ocean offshore and arctic engineering, Honolulu, Hawaii, USA; 2009.
[6] Wang KP, Xue HX, Tang WY, Guo JT. Fatigue analysis of steel catenary riser at the touch-down point based on linear hysteretic riser-soil interaction model. Ocean Eng 2013;68:102–11.
[7] Aubeny C, Gaudin C, Randolph M. Cyclic tests of model pipe in kaolin. In: Offshore technology conference, Houston, Texas, USA; 2008.
[8] Hodder MS, White DJ, Cassidy MJ. Centrifuge modelling of riser-soil stiffness degradation in the touchdown zone of a steel catenary riser. In: Proceedings of the ASME 27th international conference on offshore mechanics and arctic engineering, Estoril, Portugal; 2008.
[9] Bradley JE, Arash Z, Andrew M. Centrifuge modeling of steel catenary risers at touch down zone part I: development of novel centrifuge experimental apparatus. Ocean Eng 2013;60:200–7.
[10] Bradley JE, Arash Z, John B. Centrifuge modeling of steel catenary risers at touch down zone part II: assessment of centrifuge test results using kaolin clay. Ocean Eng 2013;60:208–18.
[11] DNV. Deep water coupled floater motion analysis (DeepC Theory)[M]. 2005. Norway.
[12] Blevins RD. Flow-induced vibrations. New York: Van Nostrand Reinhold; 1990.
[13] Jauvtis N, Williamson CHK. The effect of two degrees of freedom on vortex-induced vibration at low mass and damping. J Fluid Mech 2004;509:23–62.
[14] Stappenbelt B, Lalji F, Tan G. Low mass ratio vortex-induced motion. In: 16th Australasian fluid mechanics conference, Crown Plaza, Gold Coast, Australia; 2007.
[15] Blevins RD, Coughran CS. Experimental investigation of vortex-induced vibration in one and two dimensions with variable mass, damping, and Reynolds number. J Fluids Eng 2009;131:101202.
[16] Trim AD, Braaten H. Experimental investigation of vortex-induced vibration of long marine risers. J Fluids Struct 2005;21:335–61.
[17] Vandiver JK, Swithenbank SB, Jaiswal V. Fatigue damage from high mode number vortex-induced vibration. In: Proceedings of the 25th international conference on offshore mechanics and arctic engineering, Hamburg, Germany; 2006.
[18] Vandiver JK, Swithenbank S, Jaiswal V. The effectiveness of helical strakes in the suppression of high-mode-number VIV. In: Offshore technology conference, Houston, Texas, USA; 2006.
[19] Wang JG, Fu SX, Baarholm R. Fatigue damage of a steel catenary riser from vortex-induced vibration caused by vessel motions. Mar Struct 2014;39:131–56.
[20] Fang SM, Niedzwecki JM, Fu SX. VIV response of a flexible cylinder with varied coverage by buoyancy elements and helical strakes. Mar Struct 2014;39:70–89.
[21] Vandiver JK, Li L. SHEAR7 V4.4 program theory manual. Cambridge, USA: Department of Ocean Engineering, MIT; 2004.
[22] Larsen CM, Vikestad K, Yttervik R. VIVANA – theory manual. Norway: Norwegian Marine Technology Research Institute; 2005.
[23] Baarholm GS, Larsen CM, Lie H. On fatigue damage accumulation from in-line and cross-flow vortex-induced vibrations on risers. J Fluids Struct 2006;22:109–27.
[24] Finn L, Lambrakos K, Maher J. Time domain prediction of riser VIV. In: 4th international conference on advances in riser technologies; 1999. Aberdeen.
[25] Sidarta DE, Finn LD, Maher J. Time domain FEA for riser VIV analysis. In: Proceedings of the 29th international conference on offshore mechanics and arctic engineering. Shanghai, China; 2010.
[26] Larsen CM, Passano E. Time and frequency domain analysis of catenary risers subjected to vortex induced vibrations. In: Proceedings of the 25th international conference on offshore mechanics and arctic engineering, Hamburg; 2006.
[27] Wang KP, Xue HX, Tang WX. Time domain prediction approach for cross-flow VIV induced fatigue damage of steel catenary riser near touchdown point. Appl Ocean Res 2013;43:166–74.
[28] Gopalkrishnan R. Vortex induced forces on oscillating bluff cylinders. Cambridge, MA, USA: Department of Ocean Engineering, MIT; 1993.
[29] Aronsen KH, Larsen CM. Hydrodynamic coefficients for in-line vortex induced vibrations. In: Proceedings of the ASME 26th international conference on offshore mechanics and arctic engineering, San Diego, California, USA; 2008.
[30] Venugopal M. Damping and response of a flexible cylinder in a current. Cambridge, USA: Department of Ocean Engineering, MIT; 1996.
[31] Lie H, Kaasen KE. Modal analysis of measurements from a large-scale VIV model test of a riser in linearly sheared flow. J Fluids Struct 2006;22:557–75.
[32] DNV. Fatigue design of offshore steel structures. 2010. DNV-RP-C203.
[33] 2H Offshore Engineering Ltd. STRIDE JIP – effect of riser/seabed interaction on SCRs. Report No. 1500-RPT-008. 2002.
[34] Bridge CD, Howells HA. Observations and modeling of steel catenary riser trenchs. In: The international ocean and polar engineering conference, Lisbon, Portugal; 2007.